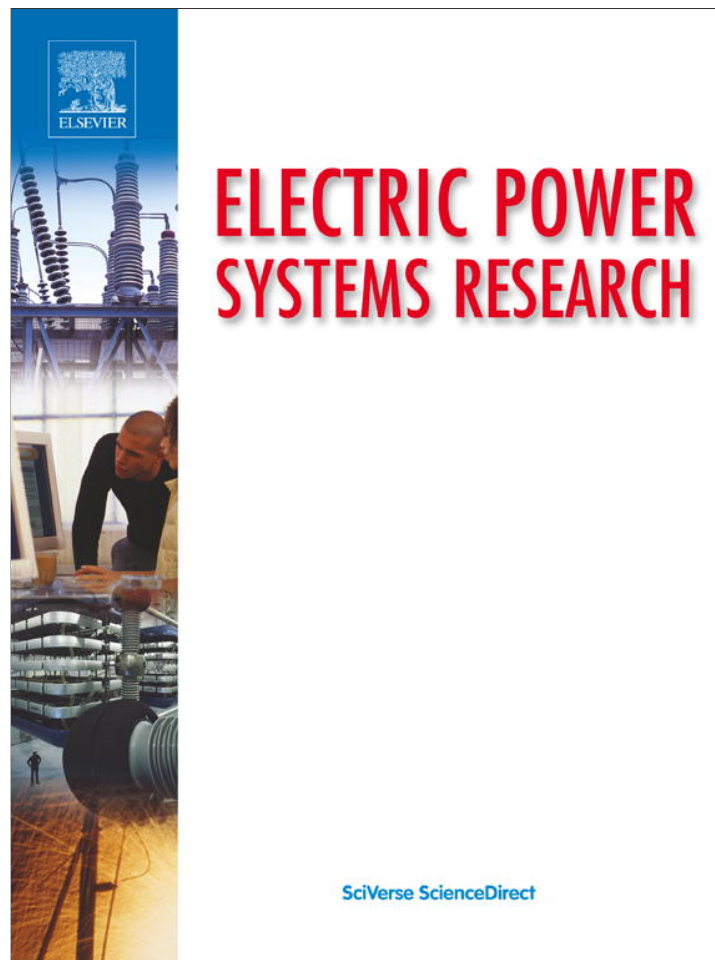


Provided for non-commercial research and education use.
Not for reproduction, distribution or commercial use.



(This is a sample cover image for this issue. The actual cover is not yet available at this time.)

This article appeared in a journal published by Elsevier. The attached copy is furnished to the author for internal non-commercial research and education use, including for instruction at the authors institution and sharing with colleagues.

Other uses, including reproduction and distribution, or selling or licensing copies, or posting to personal, institutional or third party websites are prohibited.

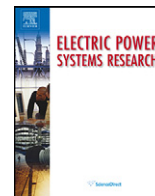
In most cases authors are permitted to post their version of the article (e.g. in Word or Tex form) to their personal website or institutional repository. Authors requiring further information regarding Elsevier's archiving and manuscript policies are encouraged to visit:

<http://www.elsevier.com/copyright>



Contents lists available at SciVerse ScienceDirect

Electric Power Systems Research

journal homepage: www.elsevier.com/locate/epsr

Mathematical modeling of flashover mechanism due to deposition of fire-produced soot particles on suspension insulators of a HVTL

Emad H. El-Zohri^{a,*}, M. Abdel-Salam^b, Hamdy M. Shafey^c, A. Ahmed^b

^a Electrical Engineering Department, Faculty of Industrial Education, Sohag University, Sohag, Egypt

^b Electrical Engineering Department, Faculty of Engineering, Assiut University, Assiut, Egypt

^c Mechanical Engineering Department, Faculty of Engineering, Assiut University, Assiut, Egypt

ARTICLE INFO

Article history:

Received 4 January 2012

Received in revised form 11 August 2012

Accepted 17 September 2012

Keywords:

Mathematical modeling of agricultural fires

Soot deposition

Fire-induced-flashover

ABSTRACT

This paper presents a mathematical integrated model that simulates the coupled events causing flashover due to the deposition of soot particles on suspension insulators of high voltage transmission lines (HVTL). The model considers non-steady three-dimensional multi-phase flow of agricultural fire producing the soot particles. In addition, the model describes in detail the mechanism of the soot deposition combined with the developing of the electric field. The model equations are simultaneously solved using an iterative finite-volume numerical technique together with the indirect boundary element and charge simulation methods. The model validity and accuracy are verified through the discussion of the results for a representative case study of a 15 kV cap-and-pin insulator string. The discussion includes a comparison of the present numerical predictions for characteristics of the deposited soot layer, electric field distribution, and characteristics of flashover occurrence, with the available results in the literature.

Crown Copyright © 2012 Published by Elsevier B.V. All rights reserved.

1. Introduction

High voltage transmission lines (HVTL) usually cross agricultural fields in which accidental fires may occur. Also, farmers intentionally burn crop residues in such agricultural fields as a harvesting aid. The occurring agricultural fires result in environmental impact represented by thermal and gaseous pollution accompanied with the production of soot particles. The soot particles deposited on the insulator surface of the high voltage transmission lines are often reported to cause flashover and consequently, the outages of these lines. In some tropical countries, the number of line outages due to fires, whether intentional or accidental, can be up to hundreds a year per line [1]. This leads to a great economic loss for both the utility and users.

Accurate modeling of the flashover mechanism requires deep understanding and appropriate formulation of the equations governing the physical and chemical processes associated with combustion, spread of fire, and deposition of fire-produced soot particles. The presence of electric field of the energized transmission line affects the flow and deposition of soot particles as the solid phase of the multi-phase flow of the fire products. The deposited soot layer results in an increasing leakage current over the

insulator surface which by turn leads to the flashover of high voltage insulators.

Most of the published works [2–6] on mathematical modeling of combustion and fire spread were generally limited due to simplifying assumptions which cannot be extended to many of the real cases. Recently, the present authors developed a more realistic mathematical three-dimensional non-steady fire model [7] as a preparatory stage of the present work.

The research works on topics related to fire spread investigate models and measurements of turbulent gas–particle flow and the soot particles deposition [8–10]. Current approaches commonly used to simulate turbulent gas–particle flow in computational fluid dynamics (CFD) are the Eulerian–Eulerian and the Eulerian–Lagrangian models [11,12]. In the Eulerian–Eulerian approach, both the gas and particle flows are treated as continuous fluid flow and regarded as interacting with each other. In the Eulerian–Lagrangian approach, the Eulerian equations of the gas phase are solved and the Lagrangian equations of particle motion are integrated by tracking individual particle through the flow field. Tian [13] investigated the performance of the two gas–particle models, and developed particle-wall collision models describing the associated boundary conditions. Zhang and Chen [14] used a modified Lagrangian method to predict particle deposition onto indoor surfaces. Valentine and Smith [15] described a model coupled with a particle cloud tracking technique for predicting particle deposition in turbulent flow fields. Cohan [16] experimentally

* Corresponding author. Tel.: +20 88 2299037; fax: +20 88 332553.

E-mail address: emad.elzohri@yahoo.com (E.H. El-Zohri).

Nomenclature

a	absorption coefficient the gas/soot mixture, m^{-1}
A, B, C	cosine directions of a vector
D_ϕ	the effective diffusion coefficient of any transported variable ϕ
E	magnitude of electric field strength, $V m^{-1}$
f_{vs}	soot volume fraction
g_i	gravity vector, $m s^{-2}$
h	enthalpy of the gas mixture, $J kg^{-1}$
Δh	heat of reaction, $J kg^{-1}$
I	current, A
J	irradiance, $W m^{-2}$
k	turbulent kinetic energy, $m^2 s^{-2}$
m_p^{acc}	mass of accumulated soot particles, kg
p	pressure of the gas mixture, Pa
Pr	Prandtl number
Q_i	discrete charges, C
R	resistance, Ω
\bar{R}	universal gas constant
Re	Reynolds number
Sc	Schmidt number
t	time, s
T	temperature of the gas mixture, K
T_{SL}	temperature of soot layer, K
u_i	velocity vector of gas phase, $m s^{-1}$
u_{p_i}	velocity vector of soot particles, $m s^{-1}$
V_p	electric potential at any point p , V
x, y, z	Cartesian coordinates in tensor notation
Y	mass fraction

Greek symbols

δ_{SL}	soot layer thickness, m
ε	turbulent kinetic energy dissipation rate
ψ	surface charge density, $C m^{-2}$
μ	viscosity
$\dot{\omega}$	reaction or process rate, $kg m^{-3} s^{-1}$
ϕ	any transported variable
ρ	density of the gas phase
ρ_p	density of the soot particles
σ	Stephan–Boltzmann constant
σ_ϕ	turbulent Prandtl/Schmidt number for any transported variable ϕ
σ_{SL}	electric conductivity of soot layer, $S m^{-1}$
τ	time constant
θ	incident angle of soot particles

Subscripts and superscripts

α	gas species ($\alpha = CO, CO_2, O_2, H_2O$ and N_2)
∞	free stream value
L	leakage path length, m
n	normal component
p	soot particles
ϕ	any transported variable
t	tangential component
SL	soot layer

validated a more specific model for the soot deposition in fire dynamics simulator (FDS). Important factors in soot deposition modeling are the particle deposition velocity and soot material properties. These factors can be determined using measurements, models, and properties in different published works [8,17,18].

Numerous works have been devoted to understand the phenomena leading to flashover of polluted insulators in order to

elaborate a model allowing one to predict accurately the critical flashover voltage. A common limitation for most proposed models [19–23] is the simplified static representation of propagating arc in series with the resistance of the polluted layer. Proposed models in the last three decades individually considered various parameters such as arc dynamics [24–28], the chemical nature of the pollutants [29], and multiple arcs [30]. The discussed published works are valuable as a first simple approach for the separate topics (fire model, soot deposition, and flashover mechanism) involved in the real complex case of fire-induced flashover.

The aim of the present work is to formulate and solve a non-steady three-dimensional mathematical integrated model for the flashover mechanism due to the deposition of fire-produced soot particles on high voltage insulators. This model accurately simulates the coupled real events of the multi-phase flow produced by agricultural fires occurring beneath a high voltage transmission line. Also, the model introduces a detailed treatment of soot particles deposition on the insulator string units with a precisely described geometry. The features of this geometry are key factors in flow and deposition of soot particles, electric field distribution, and consequently, flashover criterion. The model equations are simultaneously solved using an iterative finite-volume numerical technique together with charge simulation and indirect boundary element methods for calculating the electric field distribution. Model numerical predictions are presented and discussed for a representative case study to check the model validity and accuracy. These predictions include characteristics of the deposited soot layer, electric field distribution, and characteristics of flashover occurrence.

2. Mathematical formulation

The present mathematical model analyzes the transport phenomena including fire products leading to the flashover, specifies the conditions for the agricultural fire model, and describes the transmission line insulator boundary and the associated processes occurring at this boundary. The model includes the basic system of differential and integral equations that govern the transport phenomena, with corresponding initial and boundary conditions. The model equations are simultaneously solved using an iterative finite-volume numerical technique. The following sub-sections describe the details of the present mathematical model.

2.1. Theoretical model and basic assumptions

Fig. 1 shows the important features describing the theoretical model including the agricultural fire model and the insulator string model. The figure shows the coordinate system, dimensions, and the associated outer boundaries of the whole computational domain. A wind-driven fire propagates in the agricultural fuel bed of a depth δ_M , width W_M , and length L_M forming a fire model with a flame of a height H_M . The wind flow is in the x -direction with a vertical velocity distribution as shown in Fig. 1. The dimensions of the whole computational domain are mainly expressed in terms of those for the conceptual structure representing the agricultural fire model. These selected dimensions are large enough to agree with the practical considerations of computational fluid dynamics (CFD) for wind environment around structures [31]. The insulator string consisting of N identical rotationally symmetric units is stressed by a system voltage V_{system} at a height H_{st} with respect to the ground plane. The vertical axis of the insulator string is located in the symmetry plane of the whole computational domain, at a horizontal length L_{st} from the fire model. Usually, the height H_M of the occurring fire beneath the transmission line is less than the height H_{st} with enough distance resulting in small values of the electric field

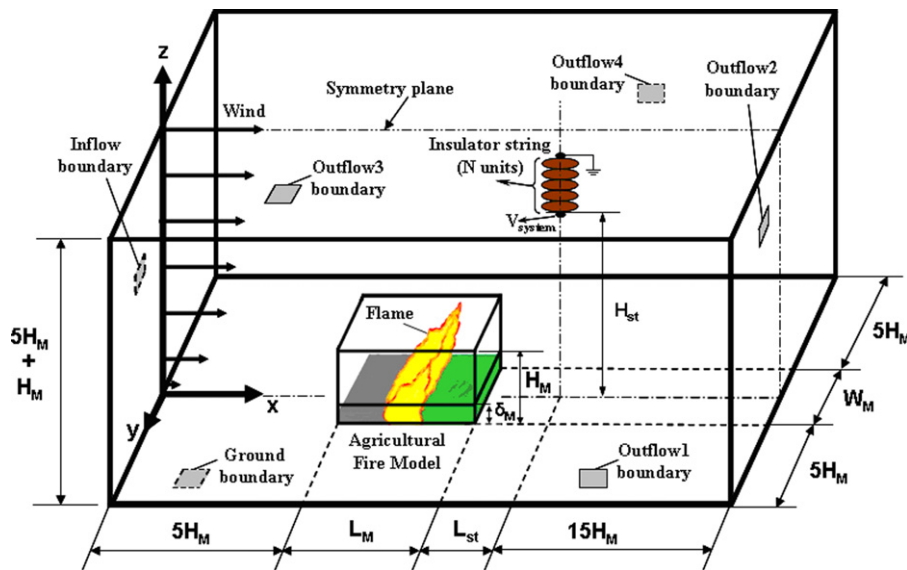


Fig. 1. General features and dimensions of the computational domain including the agricultural fire model and the insulator string of the transmission line.

at vertical levels down to H_M . The following basic assumptions are considered in the present mathematical formulation.

- (1) Added to the stated wind direction and location of the insulator string axis, the agricultural fuel bed usually has uniform structure and properties. Accordingly, the spatial variations of the flow properties are considered identical around the symmetry plane of the whole computational domain.
- (2) The effect of the electric field can be neglected in the space down to the flame height H_M . Accordingly, in this space the soot particles are simply included in the gas phase of the multi-phase medium of the fire model. On the other hand, the soot particles are treated as a separate solid phase in the other space of the whole computational domain where the electric field is effective.
- (3) The continuity and momentum equations are only considered for the solid phase of the soot particles which are in thermal equilibrium with the associated gas phase. In addition, the diffusion and the turbulence terms in the momentum equations are neglected due to the small density of the solid phase compared with the gas phase density.
- (4) No chemical reactions are considered in the space of the whole computational domain above the flame height either for the carrier gas phase or for the dispersed solid phase of the soot particles.
- (5) The effects of any objects (e.g. buildings, towers, trees. . .), existing within the whole computational domain, are neglected and attention is focused only on the insulator string.

The statement of assumption (1) suggests that only half of the whole computational domain is sufficient to describe precisely the spatial variations of the whole flow, with less computations. Moreover, for easy but accurate treatment of the whole flow, half of the computational domain can be divided, according to assumption (2), into two distinct Sub-domains as shown in Fig. 2. The two Sub-domains have the common outer boundaries of inflow, outflow 1, outflow 2, and the symmetry plane. Besides these boundaries, the Sub-domain I is bounded in vertical direction by the ground boundary and the imaginary interface plane, while the Sub-domain II is bounded by the imaginary interface plane and the outflow 3 boundary. The Sub-domain I concerns with the agricultural fire model representing the multi-phase flow whose solid phase is the

stagnant agricultural solid fuel particles. On the other hand, the Sub-domain II concerns with the multi-phase flow of the fire products whose solid phase is the soot particles.

2.2. Treatment of the agricultural fire model in Sub-domain I

The fire model in the present study is represented by a multi-phase medium, including multi-class agricultural solid fuel. The model assumptions, basic equations, and associated initial and boundary conditions are formulated and presented in detail by the present authors [7]. In this model, the degradation of the solid fuel is controlled by dehydration, pyrolysis, and char oxidation processes whose reaction rates are expressed by Arrhenius-type equations. The degradation of the solid fuel is mainly characterized by the time variation of water content, dry fuel, char, and ash mass fractions. The evolution of these mass fractions besides the fuel volume fraction, density, and temperature are all governed by a set of seven first-order ordinary differential equations [7].

The flow behavior of the gas phase in the present fire model is described by the turbulence modeled balance equations for mass, momentum, energy, and chemical species mass fraction. The gas phase is a mixture resulting from the thermal degradation of the solid phase matrix and the combustion reactions. These fire processes, normally contribute soot and major five gaseous species namely, CO, CO₂, O₂, H₂O, and N₂. Therefore, mass fractions of these five gases beside the soot volume fraction have been conserved. An elliptic partial differential equation in the generic form [4–6] is used to express the balances of various flow properties for non-steady three-dimensional gas flow of the fire model.

2.3. Basic equations for the multi-phase flow of the fire products in Sub-domain II

2.3.1. Gas phase

The flow behavior of the gas phase in Sub-domain II is treated in a manner similar to that of the fire model in Sub-domain I. The gas phase in Sub-domain II is considered as a mixture of the same five combustion gases CO, CO₂, O₂, H₂O, and N₂. The soot particles are considered as the solid phase of Sub-domain II whose flow characteristics are discussed in the next sub-section. The general form

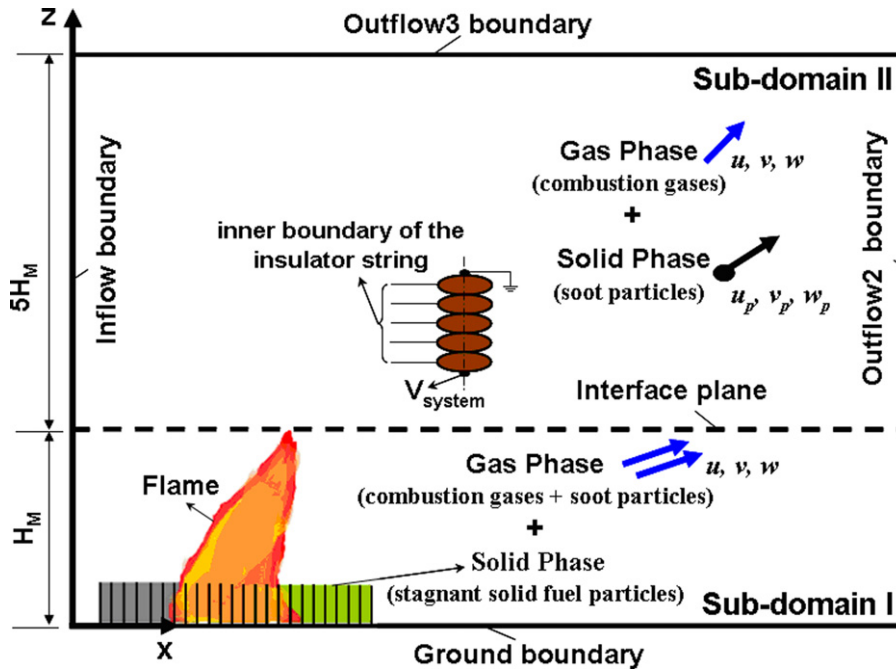


Fig. 2. Main differences between the computational sub-domains.

of the balance equations for the gas phase can be expressed by the following elliptic partial differential equation:

$$\frac{\partial(\rho\phi)}{\partial t} + \frac{\partial(\rho u_j \phi)}{\partial x_j} = \frac{\partial}{\partial x_j} \left(D_\phi \frac{\partial \phi}{\partial x_j} \right) + S_\phi, \quad (1)$$

where ϕ is the generic form of the transport fluid property having a corresponding diffusive exchange coefficient D_ϕ and a source term S_ϕ . The representation of the generic fluid property ϕ and the associated expressions for D_ϕ and S_ϕ are summarized in Table 1.

The following equation of state is used to calculate the pressure p of the gas phase assuming it a mixture of ideal gases.

$$p = \rho \bar{R} T \sum_{\alpha} \frac{Y_{\alpha}}{W_{\alpha}}, \quad (2)$$

where ρ is the gas phase density, \bar{R} is the universal gas constant, T is the gas temperature, Y_{α} is the mass fraction of gas species, and W_{α} is the molecular weight of gas species.

The last term in the source expression for momentum equations in Table 1 represents the momentum exchange between the gas phase and the solid phase with velocity components u_{p_i} . The time constant τ in this term is calculated as

$$\tau = \frac{18\mu}{\rho_p d_{\text{soot}}^2}, \quad (3)$$

where μ is the gas viscosity, ρ_p is the solid phase density, and d_{soot} is the diameter of the mono-sized soot particle, assumed to be 1 μm .

The specific enthalpy of the gas phase h is a function of the mass fractions Y_{α} and the gas temperature T , given by

$$h = \sum_{\alpha} Y_{\alpha} \left[\Delta h_{\alpha}^0 + \int_0^T C_{\alpha}(T) dT \right]. \quad (4)$$

The irradiance J appearing in the energy (specific enthalpy) equation is calculated by integrating the thermal radiation intensity in overall directions. This intensity is obtained from the solution of the three-dimensional radiative transfer equation [7].

Expressions for turbulent viscosity μ_t and the turbulence functions P_k , W_k , and R are found elsewhere [6].

The constants in Table 1 have the following values.

$$C_{\varepsilon 1} = 1.42, C_{\varepsilon 2} = 1.68, C_{\varepsilon 3} = 1.5, \sigma_h = \sigma_{f_{vs}} = \sigma_{Y_{\alpha}} = 0.7, \\ \sigma_k = 0.7179, \sigma_{\varepsilon} = 1.3, Sc = Pr = 0.71.$$

2.3.2. Solid phase

The dispersed mono-sized soot particles representing the solid phase can be treated as a quasi-fluid continuum [13] of a density ρ_p , flowing with velocity components u_{p_i} . The flow behavior of this solid phase is controlled by the following continuity and momentum equations, in tensor notation.

$$\frac{\partial \rho_p}{\partial t} + \frac{\partial(\rho_p u_{p_j})}{\partial x_j} = 0 \quad (5)$$

$$\frac{\partial(\rho_p u_{p_i})}{\partial t} + \frac{\partial(\rho_p u_{p_j} u_{p_i})}{\partial x_j} = \rho_p g_i + \tau \rho_p (u_i - u_{p_i}) + \varepsilon_0 \frac{\partial E^2}{\partial x_i} \quad (6)$$

The right hand side of Eq. (6) consists of three source terms representing the gravitational force, the drag force (momentum exchange), and the electrophoretic force with E is the magnitude of electric field strength and ε_0 is the dielectric constant of air.

2.4. Initial, outer boundary, and continuity conditions for Sub-domain II

2.4.1. Initial conditions

The initial conditions in Sub-domain II represent the values of the flow properties for both gas and solid phases, just at the beginning instant of the fire (at $t=0$) when the flow properties are those for the free stream. Thus, the initial conditions can be summarized as in Table 2.

2.4.2. Outer boundary and continuity conditions

In the present work, the outer boundaries are planes (Fig. 1) enclosing the whole computational domain. The inner boundary is represented by the surfaces of the insulator string units (Fig. 2).

Table 1
Summary of the conservation equations, Eq. (1), for gas phase expressed in the generic form.

Fluid flow property	ϕ	D_ϕ	S_ϕ
Mass	1	0	0
Momentum	u_i	$\mu + \mu_t$	$-\frac{\partial p}{\partial x_i} + \rho g_i - \frac{2}{3} \frac{\partial}{\partial x_j} \left[\left(\mu_{\text{eff}} \frac{\partial u_k}{\partial x_k} - \rho k \right) \delta_{ij} \right] + \frac{\partial}{\partial x_j} \left(\mu_{\text{eff}} \frac{\partial u_j}{\partial x_i} \right) - \tau \rho_p (u_i - u_{p_i})$
Specific enthalpy	h	$\frac{\mu}{Pr} + \frac{\mu_t}{\sigma_h}$	$a_g (J - 4\sigma T^4)$
Kinetic energy of turbulence	k	$\mu + \frac{\mu_t}{\sigma_k}$	$P_k + W_k - \rho \varepsilon$
Rate of dissipation of turbulent energy	ε	$\mu + \frac{\mu_t}{\sigma_\varepsilon}$	$(C_{\varepsilon 1} - R) \frac{\varepsilon}{k} P_k - C_{\varepsilon 2} \rho \frac{\varepsilon^2}{k} + C_{\varepsilon 3} \frac{\varepsilon}{k} W_k$
Species mass fraction	Y_α	$\frac{\mu}{Sc} + \frac{\mu_t}{\sigma_{Y_\alpha}}$	0

Table 2
Initial conditions of flow properties in Sub-domain II.

Gas phase	Solid phase
$u = v = w = 0, T = T_\infty, Y_{CO} = Y_{CO,\infty}, Y_{CO_2} = Y_{CO_2,\infty}, Y_{O_2} = Y_{O_2,\infty}, Y_{H_2O} = Y_{H_2O,\infty}, p = p_\infty, Y_{N_2} = 1 - (Y_{CO,\infty} + Y_{CO_2,\infty} + Y_{O_2,\infty} + Y_{H_2O,\infty}), \varepsilon = 10^{-6} \text{ m}^2 \text{ s}^{-3}, k = 10^{-6} \text{ m}^2 \text{ s}^{-2}.$	$\rho_p = 0, u_p = v_p = w_p = 0.$
The initial value of the gas density (ρ) is deduced using the equation of state of the ideal gas.	

In this sub-section the outer boundary conditions and the common conditions at the interface plane (continuity conditions) are discussed and formulated. The description and formulation of the inner boundary conditions are discussed in detail in Section 2.5. The conditions at the five outer planes bounding the Sub-domain II can be formulated in the following manner as shown in Table 3. The common continuity conditions at the interface plane are formulated and stated in Table 4.

2.5. Inner boundary conditions at the insulator string

This sub-section is devoted for satisfactory modeling of the insulator boundary geometry, as well as thorough description of various processes occurring at this boundary. The detailed discussion on the insulator boundary enables accurate simulation of the corresponding boundary conditions affecting the multi-phase flow

Table 3
Outer boundary conditions of flow properties in Sub-domain II.

Boundary name and geometry ^a	Boundary conditions
Symmetry: $0 \leq x \leq L_C, y = 0, H_M < z \leq H_C$	$v = 0, v_p = 0, \frac{\partial \phi}{\partial y} = 0$ for $\phi \neq v,$ $\frac{\partial u_p}{\partial y} = \frac{\partial w_p}{\partial y} = 0, \frac{\partial \rho_p}{\partial y} = 0$
Outflow 1: $0 \leq x \leq L_C, y = \frac{W_C}{2}, H_M < z \leq H_C$	$p = p_\infty, \frac{\partial \phi}{\partial y} = 0$ for all $\phi,$ $\frac{\partial u_p}{\partial y} = \frac{\partial v_p}{\partial y} = \frac{\partial w_p}{\partial y} = 0, \frac{\partial \rho_p}{\partial y} = 0$
Outflow 2: $x = L_C, 0 \leq y \leq \frac{W_C}{2}, H_M < z \leq H_C$	$p = p_\infty, \frac{\partial \phi}{\partial x} = 0$ for all $\phi,$ $\frac{\partial u_p}{\partial x} = \frac{\partial v_p}{\partial x} = \frac{\partial w_p}{\partial x} = 0, \frac{\partial \rho_p}{\partial x} = 0$
Outflow 3: $0 \leq x \leq L_C, 0 \leq y \leq \frac{W_C}{2}, z = H_C$	$p = p_\infty, \frac{\partial \phi}{\partial z} = 0$ for all $\phi,$ $\frac{\partial u_p}{\partial z} = \frac{\partial v_p}{\partial z} = \frac{\partial w_p}{\partial z} = 0, \frac{\partial \rho_p}{\partial z} = 0$
Inflow: $x = 0, 0 \leq y \leq \frac{W_C}{2}, H_M < z \leq H_C$	$v = w = 0, Y_\alpha = Y_{\alpha,\infty}, T = T_\infty, p = p_\infty,$ $u_p = v_p = w_p = 0, \rho_p = 0,$ Equations of reference [6] are used to calculate the air inflow properties; $u, k,$ and ε in terms of surface roughness z_0 and wind velocity U_w at a given height $H_w.$

^a $L_C = 5H_M + L_M + L_{st} + 15H_M, W_C = 5H_M + W_M + 5H_M, H_C = H_M + 5H_M.$

inside Sub-domain II. The discussion also focuses on the analysis towards the main target of the present work, namely, deposition of soot particles (solid phase) and the associated flashover mechanism.

2.5.1. Description of the insulator geometry

The insulator string consists of N identical units connected to each other as shown in Figs. 1 and 2 whose surfaces represent the insulator boundary. Consequently, a representative geometric description of the surface for one unit is demonstrated. Fig. 3 shows the main features of the geometry for the unit model. The unit can be approximated by an oblate spheroid (Fig. 3a). The spheroid is located at a center O' (x_u, y_u, z_u) as shown in Fig. 3b. The spheroid surface is obtained by rotating the half of an ellipse about its minor axis (z'). The angle of rotation λ ($0-2\pi$) and the angle of ellipse generation β ($-\pi/2$ to $\pi/2$) are the surface description parameters (Fig. 3b). The half-lengths a and b of the major and minor axes, respectively, are obtained from the real dimensions of the insulator unit. The formulation of the boundary conditions at the unit surface requires the mathematical description of the tangent plane and the outward normal vector with ordinate η (Appendix A) at a general point P (x', y', z') on the surface as shown in Fig. 3a.

2.5.2. Boundary conditions for the gas phase at the insulator unit surface

Considering the gas flow, the insulator represents a boundary of curved solid non-porous wall. At this boundary, the no-slip condition for the velocity components and turbulence applies. An appropriate thermal condition at the insulator surface is that the gas temperature T equals the soot layer temperature T_{SL} . The value of T_{SL} is determined later in Section 2.7. The impermeability condition is applied for the mass fractions of the gas phase species. Thus, the gas phase boundary conditions can be written as

$$u = v = w = 0, k = 0, \varepsilon = 0, p = p_\infty, T = T_{SL}, \frac{\partial Y_\alpha}{\partial \eta} = 0 \quad (7)$$

2.5.3. Boundary conditions for the solid phase at the insulator unit surface

The conditions of the solid phase particles at the insulator surface can be identified through inter-relations for the particles velocity vector and density. The application of this concept deals

Table 4
Common continuity conditions for the two sub-domains at the interface plane ($0 \leq x \leq L_C, 0 \leq y \leq \frac{W_C}{2}, z = H_M$).

Solid phase	Gas phase
$(u_p)_{II} = (u)_I, (v_p)_{II} = (v)_I,$	$(u)_{II} = (u)_I, (v)_{II} = (v)_I, (w)_{II} = (w)_I,$
$(w_p)_{II} = (w)_I, (\rho_p)_{II} = \rho_{\text{soot}}(f_{vs})_I$	$(\rho)_{II} = (\rho)_I, (Y_\alpha)_{II} = (Y_\alpha)_I, (T)_{II} = (T)_I$

Note. The subscript I refers to Sub-domain I, the subscript II refers to Sub-domain II, the soot volume fraction f_{vs} is a flow property for sub-domain I, and ρ_{soot} is the soot density.

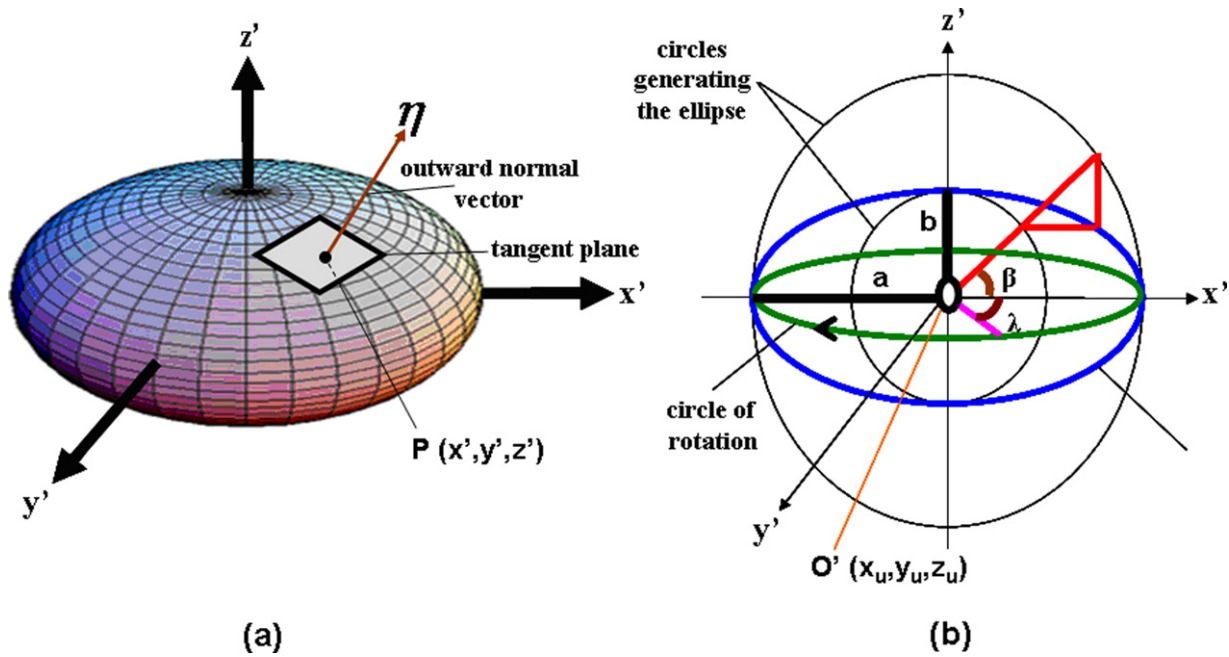


Fig. 3. Main features of the geometric model for the insulator unit: (a) the spheroid surface of the model and (b) surface parameters and dimensions.

with the choice of a control space adjacent to the specified point P on the insulator surface. Fig. 4 shows such a control space which is bounded by the tangent plane at the point P and an imaginary parallel plane at a height h (much larger than the thickness of the deposited soot layer). The soot particles arriving at the insulator surface with incident velocity vector \vec{V}_w and density $\rho_{p,w}$ suffer rebounding with restitution coefficients associated with the inward normal component $u_{n,w}^p$ and the tangential component $u_{t,w}^p$. Both incident and reflected velocities constitute the flow velocity field in the control space adjacent to the point P. Also, mass of the soot particles is conserved for this control space.

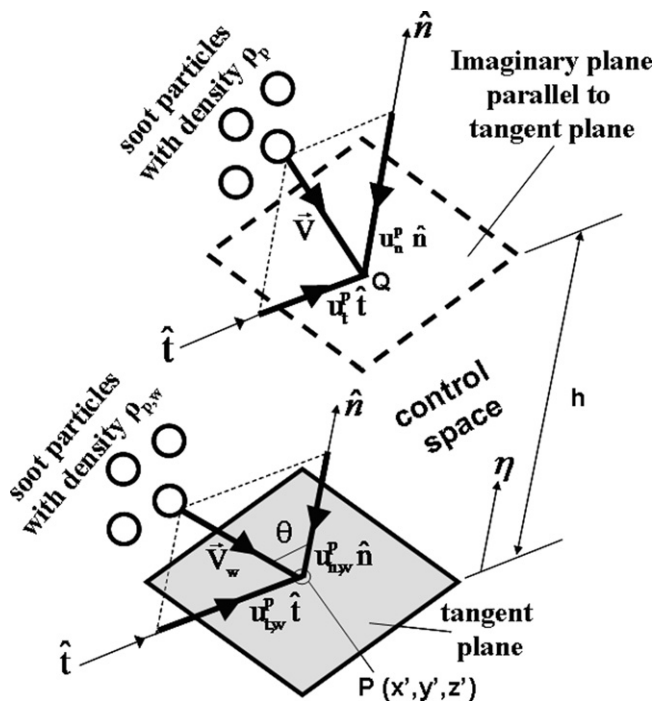


Fig. 4. The control space with the soot particle velocity vector components.

Neglecting the effect of soot deposition on mass conservation, the boundary conditions can be identified by the following generic equation [13]:

$$a\phi_w + b \frac{\partial \phi}{\partial \eta} \Big|_w = c \quad \phi = [u_n^p, u_t^p, \rho_p] \quad (8)$$

The associated coefficients a , b , and c are expressed in terms of restitution coefficients e_n and e_t . These are functions of the incident angle $\theta = \tan^{-1}(u_{t,w}^p/u_{n,w}^p)$ [13], and are given by

$$e_n = 0.993 - 1.76\theta + 1.56\theta^2 - 0.49\theta^3 \quad (9)$$

and

$$e_t = 0.988 - 1.66\theta + 2.11\theta^2 - 0.67\theta^3 \quad (10)$$

The inward normal velocity incident at the insulator surface $u_{n,w}^p$ must exceed a value known as capture velocity, u_c for the soot particles to rebound from the insulator surface. So, for $u_{n,w}^p \leq u_c$ both of the restitution coefficients e_n and e_t are equal to zero. The capture velocity u_c depends on many factors (e.g. particle size and material, insulator surface conditions...), and is to be determined experimentally. Based on the available data in the literature, a reasonable value of $u_c = 0.001 \text{ m s}^{-1}$ for soot particles is adopted [8–10]. The differential form of the generic equation (Eq. (8)) is transformed to a linear algebraic equation in the unknown ϕ_w . This is achieved by substituting for the derivative $\frac{\partial \phi}{\partial \eta} \Big|_w$ with its forward numerical formula in terms of the value of ϕ at $\eta = h$. The algebraic form of the generic equation handles the velocity components u_n^p and u_t^p . However, the coupling of the inner boundary conditions is through the Cartesian components u_{pi} used in the flow momentum equation (Eq. (6)). Thus, a two-way transformation between the two systems of velocity components must be performed (Appendix B).

2.6. Evaluation of the deposited soot layer on the insulator string

The fire-induced pollution is sensitive to the fire model parameters. These parameters include the horizontal length between insulator string and fire model (L_{st}), length of fire model (L_M), width of fire model (W_M), height of fire model (H_M), depth of fuel bed

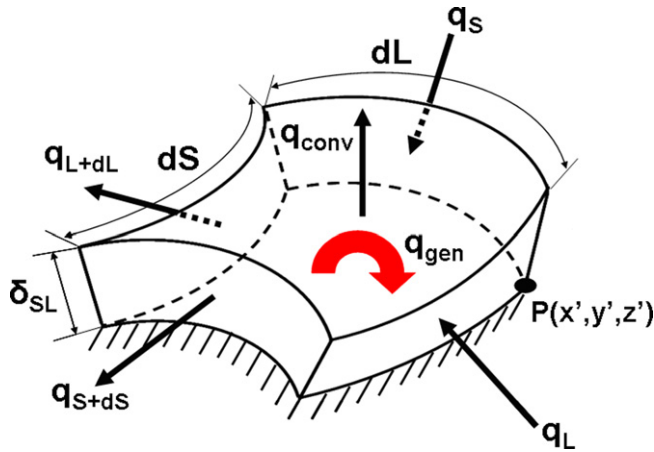


Fig. 5. The differential control volume in the soot layer and the thermal energy rates.

(δ_M), wind velocity (U_w), and initial fuel moisture content (FMC). As the dimensions of the burnt field configuration increase, the fire intensity increases and consequently, the produced-soot so that the chance for high rate of deposition increases. As the wind velocity increases, the momentum of soot particles increases so that the chance for high rate of deposition decreases. Also, as the initial fuel moisture content increases, the fire intensity decreases so that the produced-soot decreases and consequently, low deposition rate.

The soot particles with normal velocities $u_{n,w}^p$ less than or equal to the capture velocity u_c are liable to deposit on the insulator surface. Therefore, the local instantaneous deposition flux of soot particles (DF)_p can be estimated by

$$(DF)_p = \rho_{p,w} u_{n,w}^p, \quad u_{n,w}^p \leq u_c \quad (11)$$

The local instantaneous accumulated mass of deposited soot particles per unit area m_p^{acc} is calculated as

$$m_p^{acc} = \int_0^t (DF)_p dt \quad (12)$$

The local instantaneous soot-layer thickness δ_{SL} on the insulator surface is estimated as

$$\delta_{SL} = \frac{m_p^{acc}}{\rho_{SL}}, \quad (13)$$

where the soot-layer density $\rho_{SL} = (1 - \varepsilon_v)\rho_{soot}$. The voidage ratio ε_v for loose packing of soot particles can be taken as 0.45 and the bulk density of the soot material ρ_{soot} is taken to be 1800 kg m⁻³ [5].

The thermal inner boundary condition of the gas phase at the insulator surface, $T = T_{SL}$ in Eq. (7), requires accurate knowledge of the local instantaneous soot-layer temperature T_{SL} . The value of T_{SL} is a function of the soot-layer thickness δ_{SL} and varies with time and location on the insulator surface. The temperature distribution function within the deposited soot layer can be obtained in the following manner.

2.7. Temperature distribution within the deposited soot layer

Fig. 5 shows a differential control volume in the soot layer at a general point P (x' , y' , z') on the spheroid (insulator unit) surface. The control volume has a height δ_{SL} , a differential length dL , and a differential width dS . The length L is the total length on the periphery of the half-ellipses describing the profile of the insulator string units measured from the lowest point. This length is referred as

the leakage path length. The length S is the length on a circle of rotation. Expressions for the leakage path length L and the length S on the surface of the insulator string are given in Appendix A in terms of the surface description parameters β and λ . The differential control volume is exposed to different thermal energy rates with its lower surface is assumed thermally insulated as shown in Fig. 5. The thermal energy rates are classified as generation rate q_{gen} , heat transfer rates by conduction q_L , q_S , q_{L+dL} , and q_{S+dS} , and heat transfer rate by convection q_{conv} . The thermal energy generation is a result of the leakage current flowing through the soot-layer along the above-mentioned leakage path. Expressions for the heat transfer rates are derived using Fourier's law for conduction and Newton's law of cooling for convection [32]. These thermal energy rates are balanced with the rate of change of the stored energy in the differential control volume.

Applying the first law of thermodynamics on the control volume of Fig. 5 and substituting for the different energy terms by their expressions, the following two-dimensional non-steady differential heat transfer equation for the soot layer temperature T_{SL} is obtained.

$$\frac{\partial T_{SL}}{\partial t} = D_{SL} \left[\frac{1}{\delta_{SL}} \frac{\partial}{\partial L} \left(\delta_{SL} \frac{\partial T_{SL}}{\partial L} \right) + \frac{1}{\delta_{SL}} \frac{\partial}{\partial S} \left(\delta_{SL} \frac{\partial T_{SL}}{\partial S} \right) + \frac{\sigma_{SL} E_{t,L}^2}{K_{SL}} + \frac{K_{gas}}{\delta_{SL} K_{SL}} \frac{\partial T}{\partial \eta} \Big|_w \right],$$

where the thermal diffusivity of the soot layer $D_{SL} = K_{SL}/\rho_{SL} \cdot c_{SL}$, K_{SL} ($=1 \text{ W m}^{-1} \text{ K}^{-1}$) [32] is the thermal conductivity of the soot layer, c_{SL} ($=800 \text{ J kg}^{-1} \text{ K}^{-1}$) [32] is the specific heat of the soot layer, σ_{SL} is the local instantaneous electric conductivity of the soot layer, $E_{t,L}$ is the tangential component of the electric field strength along the leakage path, K_{gas} is the thermal conductivity of the gas mixture, and $\frac{\partial T}{\partial \eta} \Big|_w$ is the gas temperature gradient in the outward normal direction at the insulator surface.

The initial condition associated with Eq. (14) can be written as the insulator string surface is initially at ambient temperature T_∞ . The corresponding boundary conditions are based on two facts: symmetry conditions (at $\lambda=0$ and $\lambda=\pi$), and thermal insulation conditions at connecting points between insulator string units (at $\beta = -\pi/2$ and $\beta = \pi/2$).

The variation of the electric conductivity of the soot layer σ_{SL} with its temperature T_{SL} is obtained by

$$\sigma_{SL} = \frac{\sigma_{SL_\infty}}{[1 + \alpha_{SL} (T_{SL} - T_\infty)]} \quad (15)$$

where σ_{SL_∞} ($=1500 \text{ S m}^{-1}$) [32] is the electric conductivity of the soot layer at T_∞ , α_{SL} ($=-0.0005 \text{ K}^{-1}$) [32] is the temperature coefficient of the soot layer.

2.8. Electric field distribution

The presence of the deposited soot layer polluting the insulator surface distorts the capacitive potential distribution and the electric field is no longer capacitive but may be capacitive-resistive or resistive, depending on the severity of the surface pollution. The algorithm developed for calculating the electric capacitive-resistive field distribution is based on the indirect Boundary Element Method and the Charge Simulation Method. The insulator under investigation (Fig. 3) is surrounded by air and is stressed between a pair of electrodes (cap and pin). The top electrode is taken as grounded while the bottom electrode is stressed by the applied voltage. Since the insulator-electrodes assembly is a rotationally symmetric configuration, ring charges [33] are employed for simulation. Each electrode is simulated by a set of N_e ring charges placed within the electrode. The insulator-air interface is simulated by two sets

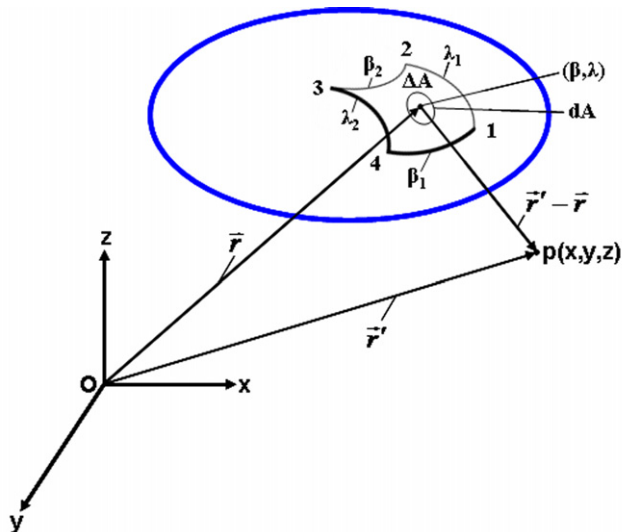


Fig. 6. Spheroidal element.

of $2N_d$ ring charges, one set placed in insulator and other set in air. Images of the fictitious ring charges with respect to the ground plane are also considered in the present algorithm. For power frequency capacitive-resistive field calculation, complex fictitious charges varying sinusoidally with time are employed to give the instantaneous field distribution [34,35]. The electrodes and insulator boundaries are discretized into several boundary elements and a suitable polynomial is introduced for the equivalent surface charges along the discrete boundary elements. Then the electric field in the region of interest is considered to be caused by the equivalent surface charges along the boundary elements. The potential $\Delta V_{p,d}$ at a space point p with ordinate \vec{r}' due to the surface charges within a finite element of area ΔA (Fig. 6) is expressed by the Fredholm integral equation of the first kind as

$$\Delta V_{p,d} = \frac{1}{4\pi\epsilon} \int_{\Delta A} \frac{\psi(\beta, \lambda)}{|\vec{r}' - \vec{r}|} dA, \quad (16)$$

where dA is the differential area centered at a surface point $P(\beta, \lambda)$ with space ordinate \vec{r} , $\psi(\beta, \lambda)$ is the corresponding surface charge density, and ϵ is the dielectric constant. The surface charge density $\psi(\beta, \lambda)$ can be expressed as a simple 4terms-polynomial [36]. Substituting for $\psi(\beta, \lambda)$, \vec{r}' , and dA in terms of β and λ , Eq. (16) can be re-written as

$$\Delta V_{p,d} = \frac{1}{4\pi\epsilon} \int_{\beta_1}^{\beta_2} \int_{\lambda_1}^{\lambda_2} \frac{(k_0 + k_1\beta + k_2\lambda + k_3\beta\lambda)(a \cos \beta \sqrt{a^2 \sin^2 \beta + b^2 \cos^2 \beta} d\beta d\lambda)}{\sqrt{(x_u + a \cos \beta \cos \lambda - x)^2 + (y_u + a \cos \beta \sin \lambda - y)^2 + (z_u + b \sin \beta - z)^2}} \quad (17)$$

The four coefficients of this polynomial (k_0, k_1, k_2 , and k_3) can be given in terms of the coordinates ($\beta_1, \beta_2, \lambda_1$, and λ_2) and the charge densities (ψ_1, ψ_2, ψ_3 , and ψ_4) of the four vertices of the element ΔA (Fig. 6). Integrating and surveying all elements of the insulator string, one can get the potential $V_{p,d}$ at the point p due to all surface charge densities as a summation over $2N_d$ unknown surface charge densities $\psi_i, i = 1, 2, \dots, 2N_d$ each multiplied by a corresponding potential coefficient function. A similar summation can be considered for the contribution of the potential $V_{p,e}$ at the point p due to $2N_e$ unknown discrete charges $Q_i, i = 1, 2, \dots, 2N_e$ simulating the electrodes. Thus the total potential V_p can be expressed as

$$V_p = V_{p,e} + V_{p,d} = \sum_{i=1}^{2N_e} P_{e,i} \cdot Q_i + \sum_{i=1}^{2N_d} P_{d,i} \cdot \psi_i, \quad (18)$$

where $P_{e,i}$ and $P_{d,i}$ are the potential coefficient functions due to discrete charges simulating the electrodes and due to surface charge densities on the insulator surface, respectively.

The electric field strength at the point p can be obtained as $\vec{E}_p = -\nabla V_p$, and the tangential component along the leakage path is given by $E_{t,L} = \partial V_p / \partial L$.

The unknown discrete charges Q_i and surface charge densities ψ_i in Eq. (18) are chosen such that they satisfy the following boundary conditions.

Dirichlet's condition on the electrode surface is

$$V_p = V_e, \quad (19)$$

where V_e is the known potential on the HV electrode and the grounded electrode with respective values of system voltage V_{system} and zero.

Potential continuity condition on the insulator-air interface (insulator surface) is

$$V_p|_{\epsilon=\epsilon_{insulator}} = V_p|_{\epsilon=\epsilon_0} \quad (20)$$

Continuity condition of the normal component of the electric flux density D_n on the insulator surface is

$$D_n|_{\epsilon=\epsilon_{insulator}} - D_n|_{\epsilon=\epsilon_0} = \psi_{true}, \quad (21)$$

where ψ_{true} is the true surface charge density. The numerical value of the true surface charge density $\psi_{true,ij}$ at a surface point p , node i, j , is calculated in terms of the potentials at the specified node and the surrounding nodes as

$$\psi_{true,ij} = \frac{1}{i\omega} \frac{1}{\Delta A_{ij}} \left[\frac{(V_p)_{i-1,j} - (V_p)_{i,j}}{R_i} - \frac{(V_p)_{i,j} - (V_p)_{i+1,j}}{R_{i+1}} + \frac{(V_p)_{i,j-1} - (V_p)_{i,j}}{R_j} - \frac{(V_p)_{i,j} - (V_p)_{i,j+1}}{R_{j+1}} \right], \quad (22)$$

where $i = \sqrt{-1}$, ω is the angular frequency, and $\Delta A_{ij} = (\Delta L \cdot \Delta S)_{ij}$ is the element surface area at the node i, j .

The resistances R_i, R_{i+1}, R_j , and R_{j+1} in Eq. (22) are calculated in terms of the local surface resistance R_{SL} at the different nodes, and the associated differences of ΔL and ΔS . The local surface resistance R_{SL} is the reciprocal of the product of the local soot layer thickness δ_{SL} and conductivity σ_{SL} .

2.9. Flashover criterion

The leakage current increases due to the accumulated deposition of the soot layer. This increase in the leakage current continues

to the extent causing start of partial arcs (discharges) along the leakage path. With further increase in the leakage current, these partial arcs elongate and join to cause flashover occurrence. This requires a condition that the arc length bridges as much as 67% of the total leakage path length [37].

The start of discharge at a specified point on the insulator surface is controlled by the arc propagation criterion ($E_{t,L} > E_{arc,L}$), where the arc electric field strength along the leakage path $E_{arc,L}$ can be expressed in terms of the leakage current I_L by

$$E_{arc,L} = AI_L^{-n} \quad (23)$$

For air environment, the arc constants take the values $A = 63$ and $n = 0.76$ [28]. The leakage current I_L can be estimated as the average

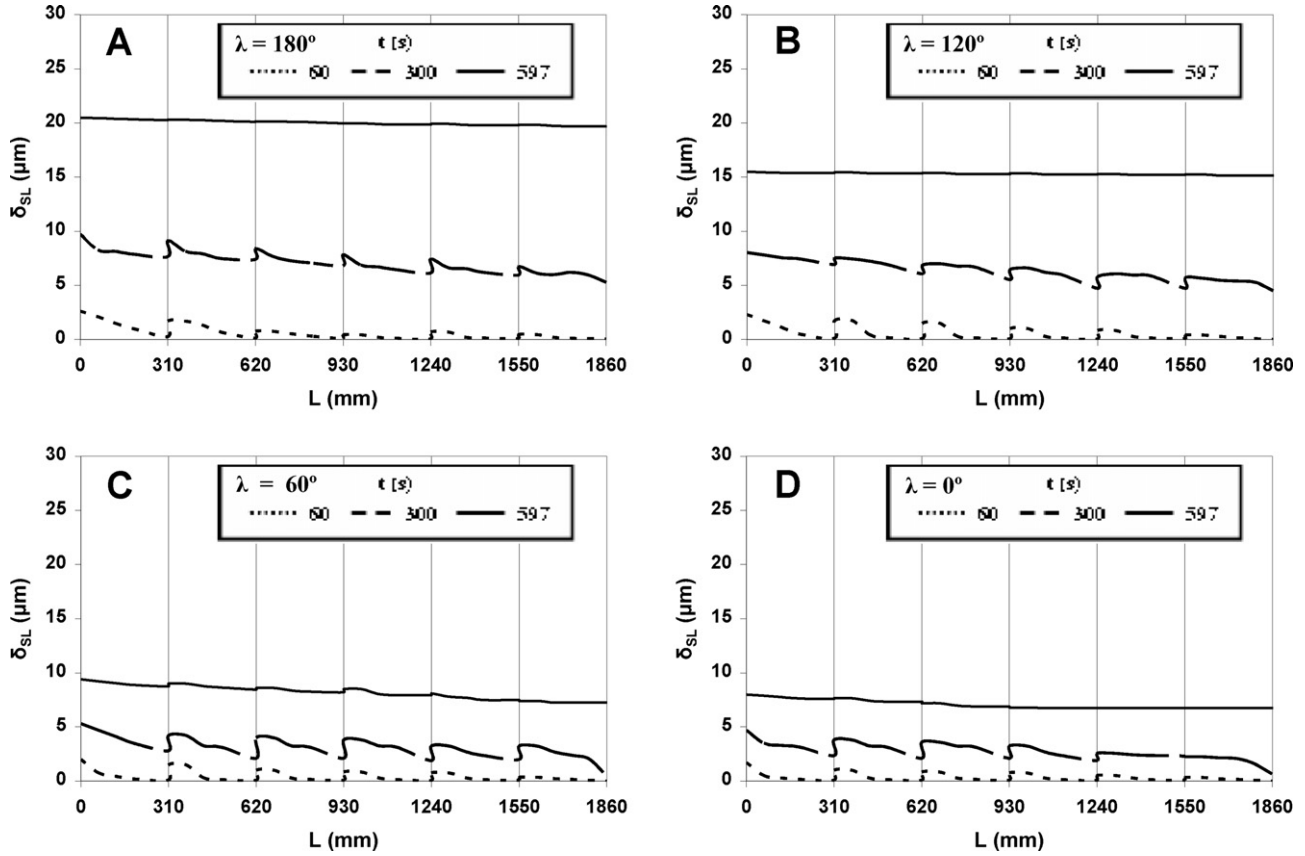


Fig. 7. Time evolution of the deposited soot layer thickness along the leakage path length for different locations on the insulator string.

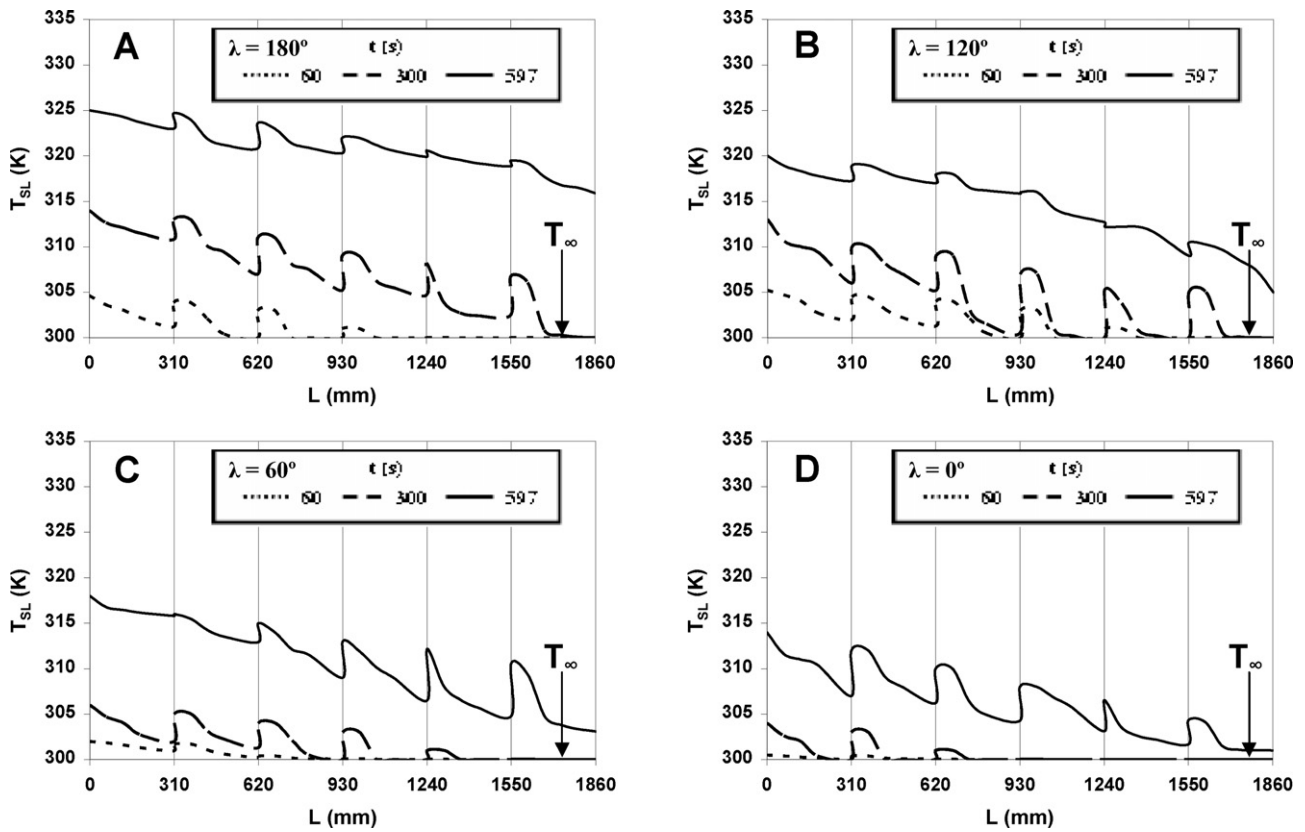


Fig. 8. Time evolution of the deposited soot layer temperature along the leakage path length for different locations on the insulator string.

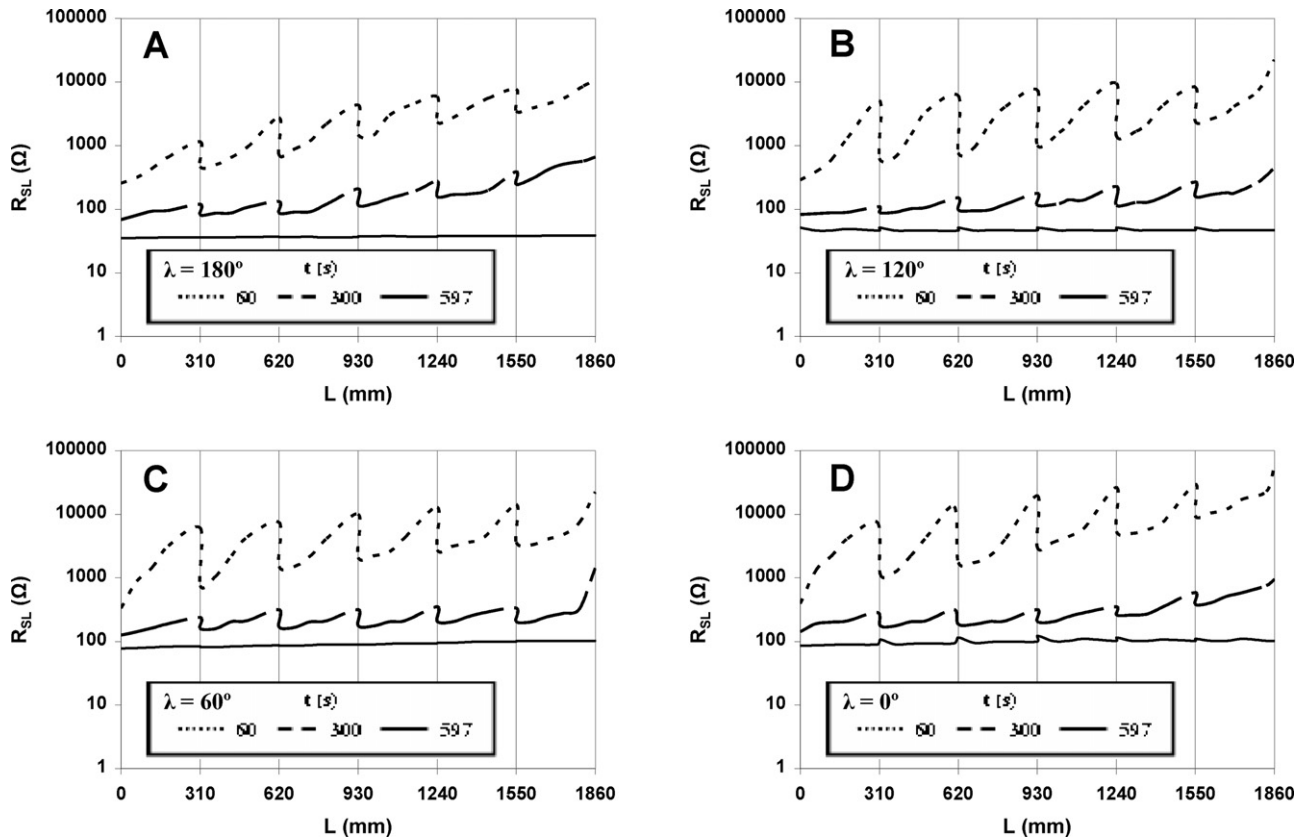


Fig. 9. Time evolution for the surface resistance of the deposited soot layer along the leakage path length for different locations on the insulator string.

of its local numerical values $I(L_i)$ (passing through finite circular rings along the leakage path), calculated by

$$I(L_i) = 2 \sum_{j=1}^m (\sigma_{SL} E_{t,L} \delta S)_{ij} \quad (24)$$

where m is the number of the j th nodes over the i th finite ring and $(\Delta S)_{ij}$ is the difference length on the corresponding half ring.

2.10. Numerical solution

The differential equations of the present mathematical model are simultaneously solved using an iterative finite-volume

numerical technique. The set of the first-order ordinary differential equations for the solid phase in the fire model are solved using the fourth-order Runge–Kutta method. The gas phase equations for the fire model in Sub-domain I and the gas phase equations as well as the solid phase equations in Sub-domain II are all discretized on a staggered, nonuniform cartesian three-dimensional grid of finite cells. A second-order backward Euler scheme is used for time integration. A second-order central difference scheme is used to approximate the diffusion terms. The resulting discretized equations are a system of linear algebraic equations which are solved iteratively using the line-by-line tridiagonal matrix algorithm [38]. In order to accelerate convergence, all the gas variables are under-relaxed using inertial relaxation. A discrete ordinate method is used as a part of the numerical solution for the radiative transfer equation [39]. The charge simulation method and the indirect boundary element method are used for the numerical calculation of the electric field distribution as formulated in detail in Section 2.8. Usually, it is needed to predict numerical results for a specific case within assigned time. The running of calculations is completed unless the condition of flashover occurrence is satisfied before this time.

3. Results and discussion

The present mathematical model was simulated by a computer program which has been developed and processed to test the model validity and accuracy. A representative case study of single-phase high voltage transmission line with a single insulator string is selected to perform this task. The transmission line crosses an agricultural fuel bed of natural tall grassland in which a wind-driven fire propagates. The main input data relevant to the transmission line and the agricultural fire model are listed in Table 5. The selected values of the parameters in Table 5 for simulations are

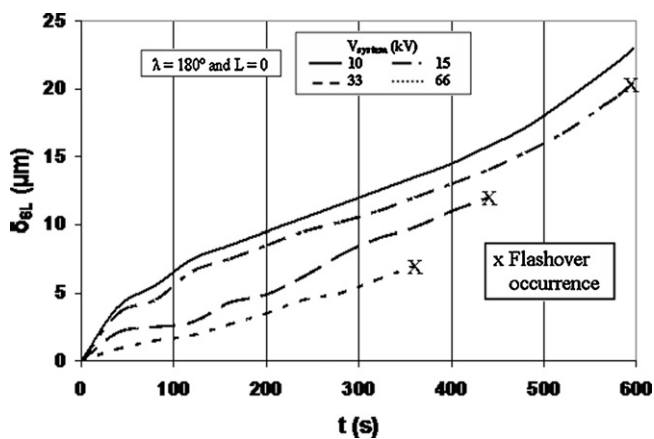


Fig. 10. Effect of varying the system voltage on the deposition of the soot layer.

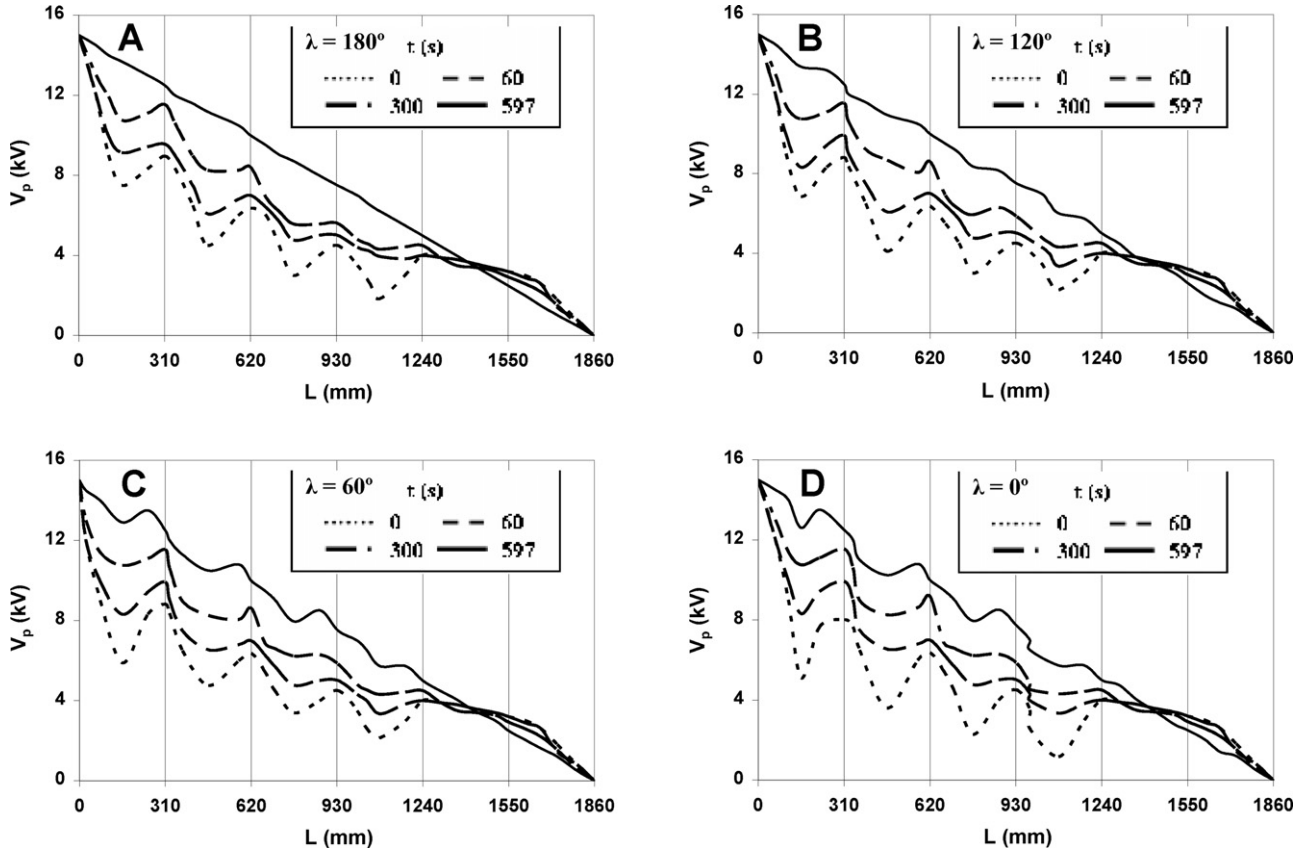


Fig. 11. Time evolution for potential along the leakage path length for different locations on the insulator string.

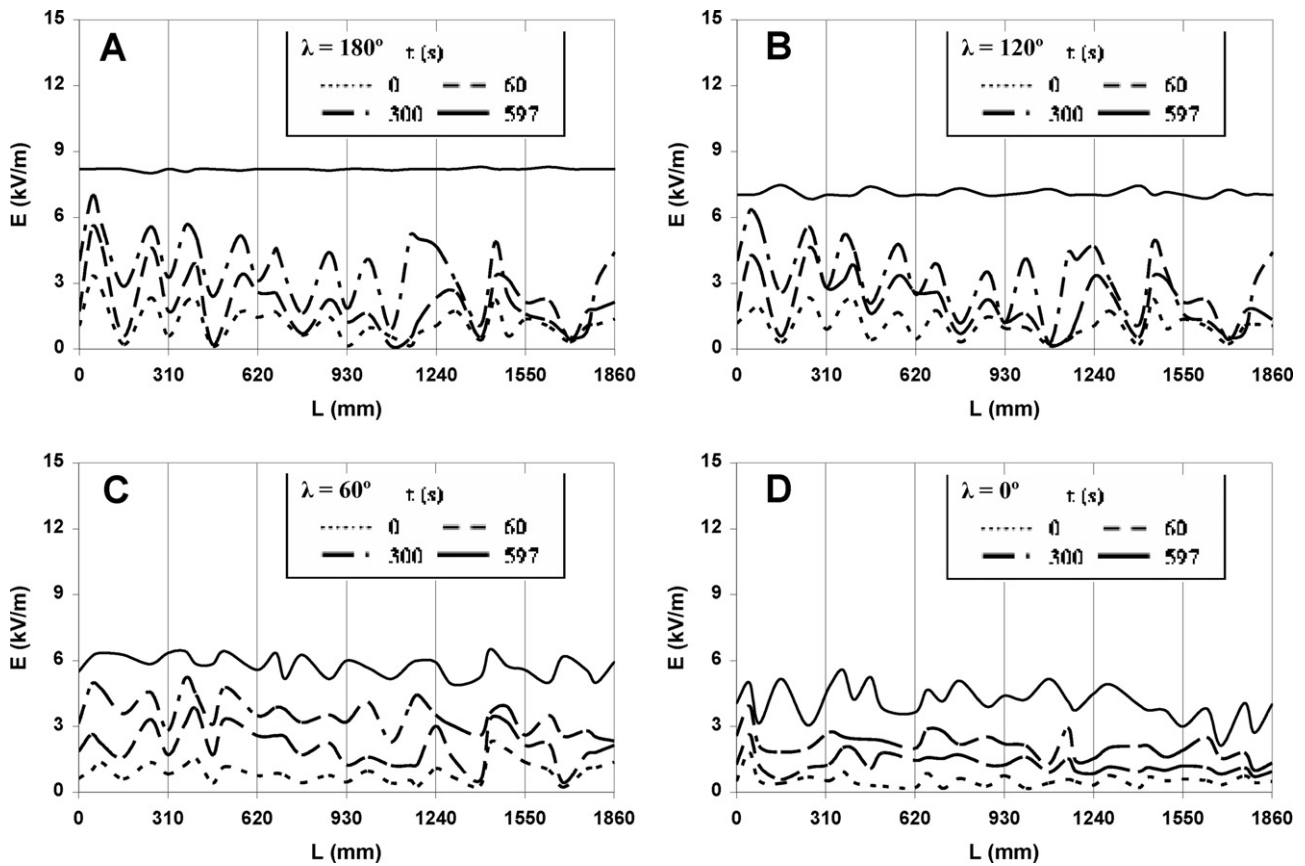


Fig. 12. Time evolution for electric field strength along the leakage path length for different locations on the insulator string.

Table 5
Main input data for the transmission line and the agricultural fire model.

Item	Value
System voltage (V_{system}), kV	15
Number of insulator string units (N)	6
Leakage path length (L_n) of an insulator string unit, mm	310
Maximum diameter ($2a$) of an insulator string unit, mm	252
Height ($2b$) of an insulator string unit, mm	146
Horizontal length between insulator string and fire model (L_{st}), m	1
Height of insulator string above the ground (H_{st}), m	9
Length of fire model (L_M), m	100
Width of fire model (W_M), m	40
Height of fire model (H_M), m	8
Fuel bed depth (δ_M), m	0.8
Wind velocity (U_w), m s^{-1}	4
Fuel Moisture Content (FMC)	0.4

encountered for common practical conditions of agricultural fires and high voltage transmission lines. The height H_M represents the maximum flame height encountered for the representative case study presented before [7]. The parameters for the transmission line are selected near enough to the fire model dimensions in order to facilitate the chance for the soot particles resulting from the fire to deposit on the insulators of the transmission line. The high value of the initial fuel moisture content, 0.4, is selected to represent the real case of plants for agricultural fields in Egypt. The data listed in Table 5 are the same for all numerical results predicted by the present model, except otherwise stated. Useful data of the fuel bed properties and the associated fire conditions are presented before [7]. A satisfactory numerical solution is obtained using a grid of $1044 \times 360 \times 348$ cells. The cells in the fuel bed region are sub-divided into a refined mesh of $200 \times 30 \times 80$ small cells. The cells adjacent to the insulator boundary are sub-divided into a refined mesh of $186 \times 6 \times 1$ small cells. In addition, a fine step of 0.025 s for time domain was taken to accelerate convergence. The convergence of the iterations for each cell is considered to be reached when the criterion $|\phi^{n+1} - \phi^n| / |\phi^n| \leq 10^{-4}$ is satisfied for a flow property ϕ . The free stream properties are $T_\infty = 300$ K, $p_\infty = 101,325$ Pa, $Y_{\text{CO}_2,\infty} = 0$, $Y_{\text{CO}_2,\infty} = 0$, $Y_{\text{O}_2,\infty} = 0.231$, and $Y_{\text{H}_2\text{O},\infty} = 0.006$. The following discussion is made on some selected model predictions which are strongly related to the soot deposition on the insulator surface and the resulting flashover characteristics.

3.1. Characteristics of the deposited soot layer

Figs. 7–10 show the results for the distribution and time evolution of the main properties (thickness, temperature, surface

resistance) of the deposited soot layer as well as the effect of system voltage on the soot layer thickness. Hereafter, a property distribution is represented by the continuous variation along the whole leakage path length for representative path lengths with A: $\lambda = 180^\circ$ (front), B: $\lambda = 120^\circ$, C: $\lambda = 60^\circ$, and D: $\lambda = 0^\circ$ (rear).

Fig. 7 shows the time evolution for the distribution of the deposited soot layer thickness. For all time instants, the soot layer thickness has large values at front leakage paths and then decreases towards the rear location. This is expected due to the combined effects of the insulator string geometry and the dominant velocity direction of the incident soot particles. For first instants ($t = 60$ s) after the beginning of the fire ($t = 0$), a non-uniformity of the soot layer thickness is noticeable from its variation along the leakage path length. The soot layer thickness approaches nearly constant values for an instant ($t = 597$ s) at which the flashover occurs. The maximum value of the soot layer thickness at which the flashover occurs is about $20 \mu\text{m}$.

Fig. 8 shows the time evolution for the distribution of the deposited soot layer temperature. Same range of temperature rise above the ambient (up to 25 K) has been reported for normally polluted insulators in the literature [40]. In [40] the temperature rise was 15 K above the ambient. A clear variation of the soot layer temperature along the leakage path is observed even at the instant of flashover ($t = 597$ s) where the soot layer thickness is nearly constant. This variation is mainly due to the variation of the tangential component of the electric field strength, $E_{t,L}$ as will be demonstrated in Fig. 14. The value of $E_{t,L}$ is a dominant factor in the thermal energy generation term controlling the rise of the soot layer temperature. Higher values of soot-layer temperature rise (up to 60 K) are expected with fires occurring at lower wind velocities and in hotter ambient.

Fig. 9 shows the time evolution for the distribution of the deposited soot-layer surface resistance. The figure indicates that the average values of the soot layer resistance ($10\text{--}100 \Omega$) are much smaller than those values presented in published works ($10^4\text{--}10^{11} \Omega$) for normally polluted insulators [41]. This is mainly due to the high value of the electric conductivity for the soot material (1500 S m^{-1} at 300 K) compared with insulator polluting materials used by other researchers having the order of $10\text{--}50 \mu\text{S m}^{-1}$. The nearly constant value of the soot-layer surface resistance along the leakage path at the time of flashover is mainly due to the nearly constant value of the soot layer thickness. The effect of the variation in the electric conductivity of the soot layer caused by the temperature rise is negligible due to small values of temperature rise shown in Fig. 8. Accordingly, the variation of the soot-layer surface resistance over the different leakage paths can be understood in the view of the variation of the soot layer thickness as shown in Fig. 7.

Fig. 10 shows the effect of varying the system voltage on the deposition of the soot layer at the beginning point of leakage path length ($L = 0$) on the front location ($\lambda = 180^\circ$). The indicated values of the system voltage represent the common rated values for transmission system voltages. The rate of soot deposition decreases and consequently, the accumulated soot layer thickness decreases as the system voltage increases. This can be explained as follows. The electric field possesses large strength values with higher system voltages. The source of momentum (Eq. (6)) in the present model accelerates most of the soot particles incident to the insulator surface resulting in less deposition rate. The figure shows that flashover occurs earlier with small soot layer thicknesses associated with higher system voltages. This is due to mainly the significant increase in the tangential component of the electric field strength and by turn, the leakage current increase. The results for lower system voltage of 10 kV show no flashover occurrence up to an assigned time of 600 s (duration of fire propagation).

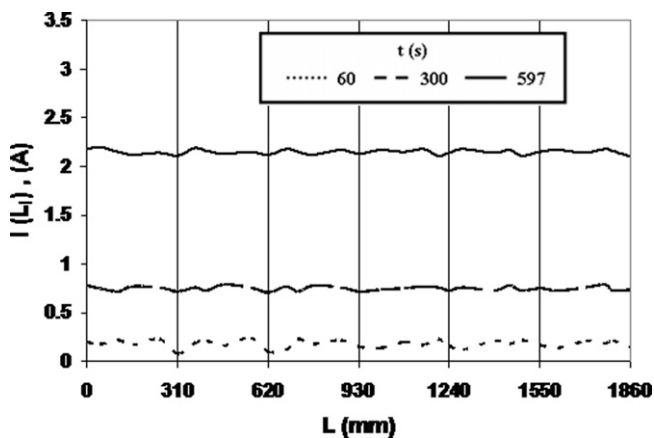


Fig. 13. Time evolution for the variation of the local leakage current along the leakage path.

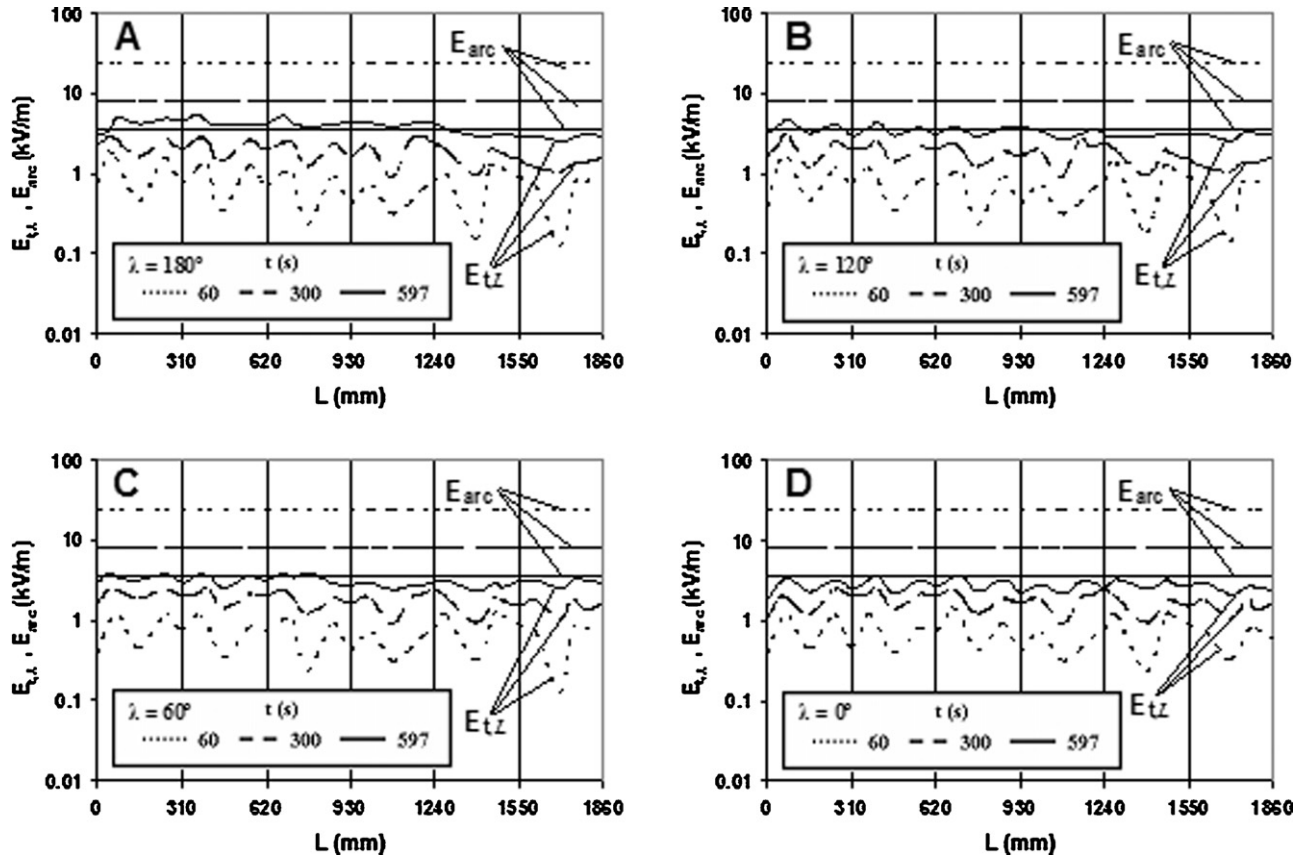


Fig. 14. Time evolution for tangential and arc electric field strength along the leakage path length for different locations on the insulator string.

3.2. Electric field distribution over the insulator surface

Figs. 11 and 12 show the results for the distribution and time evolution of the potential and the electric field strength over the insulator surface, respectively. The initial distributions shown ($t=0$) are typical for purely capacitive electric field over clean insulators commonly used with high voltage transmission lines. The distributions change with time from purely capacitive to capacitive-resistive as the surface resistance decreases gradually with the accumulation of the deposited soot layer (Fig. 9). The electric field becomes almost resistive along the leakage path when and where the flashover occurs ($t=597$ s and $\lambda=180^\circ$). The features shown in Figs. 11 and 12 of the resistive electric field are understood from the nearly linear distribution of the potential and the nearly constant value of the electric field strength along the leakage path. Similar results for artificially polluted insulators have been reported [40,41]. In [40] the value of system voltage was 15 kV as the value in this paper and the same variation is remarked. In [41] the values of potential and electric field were in per unit and the same variation is remarked.

3.3. Characteristics for flashover occurrence

Fig. 13 shows small fluctuations in the calculated local leakage current along the leakage path at different time instants. These fluctuations probably are due to numerical errors in calculating the local values of the leakage current. Therefore, it was reasonable to consider the accurate value of the leakage current as the average of its local values (Eq. (24)). The figure also shows that the leakage current increases with time till a limiting value of 2.15 A at which flashover occurs. Same range of leakage current values for flashover occurrence (0.5–3 A) has been reported even with

normally polluted insulators with pollutant resistance as high as 0.014–2 M Ω [42]. In [42], the leakage current was 2.55 A when the system voltage 33 kV. For those insulators, large electric field strengths are expected to exist with the associated large system voltages and small leakage path lengths. The resulting large values of the electric field strength combined with the large normal pollutant resistances nearly generate a situation similar to the present severely polluting case of fire-produced soot (<34 Ω).

Fig. 14 shows the time evolution for the distribution of the tangential component of the electric field strength E_{tL} and the associated values of the arc electric field strength E_{arc} . The earlier distributions of the tangential component of the electric field strength E_{tL} exhibit significant non-uniformity with maxima and minima. Then with time, the distributions become nearly uniform with increasing values. The value of E_{arc} decreases with time till it is exceeded by the value of E_{tL} along 67% of the total leakage path length at the front location ($\lambda=180^\circ$), causing the flashover to occur. This condition is not satisfied at other locations where partial arcs occur without flashover ($\lambda=120^\circ$ and 60°) or partial arcs do not occur at rear locations ($\lambda=0^\circ$). The numerical values of the tangential component of the electric field strength E_{tL} are comparable with the values reported before [40,41]. In [40] the values of tangential component of electric field were in the range from 50 to 300 kV m $^{-1}$ for the same system voltage of 15 kV but the polluting material was other than soot. In [41] the values of tangential component of electric field were in per unit and the same variation is remarked.

4. Conclusions and future work

The present study formulates and solves a non-steady three-dimensional mathematical integrated model for flashover due to

the deposition of fire-produced soot particles on high voltage insulators. The model accurately simulates the simultaneous real events involved in the multi-phase flow of fire products as well as the mechanism of soot deposition leading to the flashover. Model numerical predictions for a representative case study were presented and discussed to check the model validity and accuracy. According to the discussion of the results for the selected case study, the validity of the present model is ensured through its physically acceptable predictions. The general agreement of the present model predictions with the limited results available in the literature adds more evidence for the model validity. The discussion also emphasizes the ability of the present model to describe in detail the temporal and spatial variations of all flow properties which are necessary to be treated. These features confirm the present model accuracy in predicting the flashover characteristics for the severe case of soot pollution. The model forms a satisfactory tool in designing and dimensioning the insulators of high voltage transmission lines to avoid their expected fire-caused outages. It is expected that the predictions of the present model can be extended to cover wide range of real cases other than the present selected case. Such cases are associated with different conditions including orientation and configuration of the burnt field, shape and dimensions of the insulator string, and the existence of fire-produced solid particles other than soot. More wide application of the present model can be achieved with the addition of appropriate sub-models accounting for the general parameters affecting the mechanism of solid particles deposition on insulator surfaces. These parameters include particle shape and size distribution, accurate expression for the particle capture velocity, and insulator surface roughness.

Appendix A. Mathematical relations for the geometric description of the insulator

A point P (x', y', z') on the surface of the oblate spheroid shown in Fig. A.1 can be specified by ordinates $x', y',$ and z' (with the origin at O'), given by

$$x' = a \cos b \cos \lambda, \quad y' = a \cos b \sin \lambda, \quad \text{and} \quad z' = b \sin b \quad (\text{A.1})$$

where $x', y',$ and z' are related to the space ordinates $x, y,$ and z as

$$x' = x - x_u, \quad y' = y - y_u, \quad \text{and} \quad z' = z - z_u. \quad (\text{A.2})$$

Fig. A.1 illustrates a tangent plane at a point P on the spheroid surface and its corresponding outward normal vector. The location

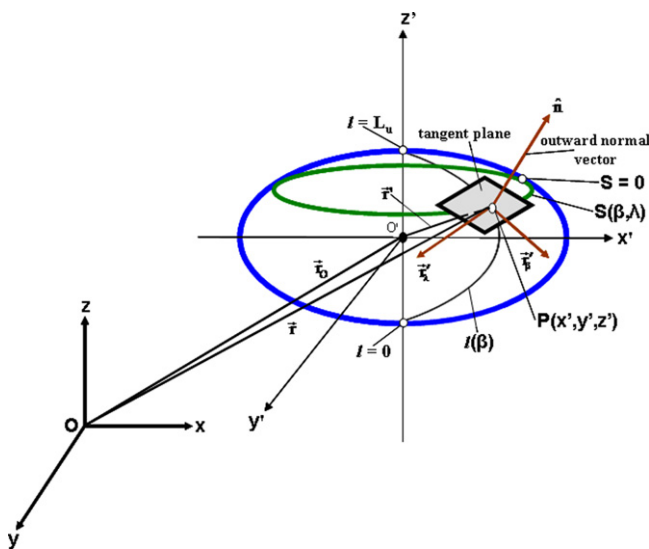


Fig. A.1. Description of the tangent plane and its normal vector in terms of the derivatives of the position vector of the point P.

of the point P can be represented alternatively using the position vector \vec{r}' as

$$\vec{r}' = x' \hat{i} + y' \hat{j} + z' \hat{k} \quad (\text{A.3})$$

where $\hat{i}, \hat{j},$ and \hat{k} are unit vectors in $x', y',$ and z' directions, respectively.

The plane tangent to the spheroid surface at point P can be represented by the two vectors \vec{r}'_β (tangent to ellipse curve) and \vec{r}'_λ (tangent to circle of rotation), given by

$$\vec{r}'_\beta = \frac{\partial \vec{r}'}{\partial \beta} \quad \text{and} \quad \vec{r}'_\lambda = \frac{\partial \vec{r}'}{\partial \lambda} \quad (\text{A.4})$$

The outward normal vector perpendicular to the tangent plane at point P can be represented by the unit vector \hat{n} given by

$$\hat{n} = \frac{\vec{r}'_\lambda \times \vec{r}'_\beta}{|\vec{r}'_\lambda \times \vec{r}'_\beta|} \quad (\text{A.5})$$

The unit vector \hat{n} can be re-expressed in terms of cosine directions $A_n(\beta, \lambda), B_n(\beta, \lambda),$ and $C_n(\beta, \lambda)$ as

$$\hat{n} = A_n(\beta, \lambda) \hat{i} + B_n(\beta, \lambda) \hat{j} + C_n(\beta, \lambda) \hat{k} \quad (\text{A.6})$$

The functions of these cosine directions can be obtained from Eqs. (A.5) and (A.6).

Referring to Fig. A.1, the length $l(\beta)$ on the half-ellipse to the point P on an insulator string unit of order j is obtained by

$$l(\beta) = \int_{-\pi/2}^{\beta} \sqrt{a^2 \sin^2 \beta + b^2 \cos^2 \beta} d\beta \quad (\text{A.7})$$

The total half-ellipse length L_u for a single insulator unit is calculated as

$$L_u = l\left(\beta = \frac{\pi}{2}\right) \quad (\text{A.8})$$

The leakage path length L is the summation of the lengths $l(\beta)$ from the lowest point on the insulator string to the specified point P and is given by

$$L = (j - 1)L_u + l(\beta) \quad (\text{A.9})$$

The length S on the circle of rotation passing the specified point P is determined by

$$S = a \lambda \cos \beta \quad (\text{A.10})$$

Appendix B. Analysis of the particle velocity vectors adjacent to the insulator surface

Consider the incident velocity vector \vec{V} of the soot particles arriving at the imaginary plane parallel to the tangent plane at the point P on the insulator surface (Fig. 4). The velocity vector \vec{V} is determined by its known cartesian components $u_p, v_p,$ and w_p as

$$\vec{V} = u_p \hat{i} + v_p \hat{j} + w_p \hat{k} \quad (\text{B.1})$$

The velocity vector \vec{V} can be written in terms of its components in the plane of incidence (inward normal component u_n^p and tangential component u_t^p) as

$$\vec{V} = -u_n^p \hat{n} + u_t^p \hat{t} \quad (\text{B.2})$$

The unknown values of u_n^p and u_t^p are determined by

$$u_n^p = -\vec{V} \cdot \hat{n} \quad \text{and} \quad u_t^p = \sqrt{|\vec{V}|^2 - (u_n^p)^2} \quad (\text{B.3})$$

The known unit normal vector \hat{n} is determined by Eq. (A.6). On the other hand, the unknown unit tangent vector \hat{t} , which is required for the reverse transformation, is determined as follows.

The unit vector \hat{t} can be written in terms of cosine directions as

$$\hat{t} = A_t(\beta, \lambda)\hat{i} + B_t(\beta, \lambda)\hat{j} + C_t(\beta, \lambda)\hat{k} \quad (\text{B.4})$$

The cosine directions $A_t(\beta, \lambda)$, $B_t(\beta, \lambda)$, and $C_t(\beta, \lambda)$ can be obtained by substituting Eq. (B.4) for \hat{t} in Eq. (B.2) and equating with Eq. (B.1).

The velocity components at the insulator surface $u_{n,w}^p$ and $u_{t,w}^p$ calculated by the generic equation (Eq. (8)) are transformed into their corresponding cartesian components by using equations from Eqs. (B.1)–(B.4) in a reverse manner.

References

- [1] A. Robledo-Martinez, E. Guzman, J.L. Hernandez, Dielectric characteristics of a model transmission line in the presence of fire, *IEEE Transactions on Electrical Insulation* 26 (4) (1991) 776–782.
- [2] G.L.W. Perry, Current approaches to modeling the spread of wildland fire: a review, *Progress in Physical Geography* 22 (2) (1998) 222–245.
- [3] D. Morvan, J.L. Dupuy, Modeling of fire spread through a forest fuel bed using a multiphase formulation, *Combustion and Flame* 127 (2001) 1981–1994.
- [4] D. Morvan, J.L. Dupuy, Modeling the propagation of a wildfire through a Mediterranean shrub using a multiphase formulation, *Combustion and Flame* 138 (2004) 199–210.
- [5] B. Porterie, J.L. Consalvi, J.C. Loraud, F. Giroud, C. Picard, Dynamics of wildland fires and their impact on structures, *Combustion and Flame* 149 (2007) 314–328.
- [6] N. Sardoy, J.L. Consalvi, B. Porterie, A.C. Fernandez-Pello, Modeling transport and combustion of firebrands from burning trees, *Combustion and Flame* 150 (2007) 151–169.
- [7] E.H. El-Zohri, H.M. Shafey, M. Abdel-Salam, A. Ahmed, Mathematical modeling of agricultural fires beneath high voltage transmission lines, *Energy* 36 (2011) 385–396.
- [8] G.N. Bae, C.S. Lee, S.O. Park, Measurements and control of particle deposition velocity on a horizontal wafer with thermophoretic effect, *Aerosol Science and Technology* 23 (3) (1995) 321–330.
- [9] A. Petroff, L. Zhang, Development and validation of a size-resolved particle dry deposition scheme for application in aerosol transport models, *Geoscientific Model Development* 3 (2010) 753–769.
- [10] A. Guha, Transport and deposition of particles in turbulent and laminar flow, *Annual Review of Fluid Mechanics* 40 (2008) 311–341.
- [11] J.Y. Tu, J.H. Yeoh, Y.S. Moris, W. Yang, A study of particle rebounding characteristics of a gas–particle flow over a curved wall surface, *Aerosol Science and Technology* 38 (2004) 739–755.
- [12] Y.S. Morsi, J.Y. Tu, J.H. Yeoh, W. Yang, Principal characteristics of turbulent gas–particulate flow in the vicinity of single tube and tube bundle structure, *Chemical Engineering Science* 59 (2004) 3141–3157.
- [13] Z.F. Tian, Numerical modeling of turbulent gas–particle flow and its applications, PhD Thesis, School of Aerospace, Manufacturing & Mechanical Engineering, RMIT University, Australia, 2006.
- [14] Z. Zhang, Q. Chen, Prediction of particle deposition onto indoor surfaces by CFD with a modified Lagrangian method, *Atmospheric Environment* 43 (2) (2009) 319–328.
- [15] J.R. Valentine, P.J. Smith, Numerical predictions of deposition with a particle cloud tracking technique, Report, Department of Chemical and Fuels Engineering, University of Utah, Salt Lake City, UT, USA, 1998.
- [16] B.D. Cohan, Verification and validation of the soot deposition model in fire dynamics simulator, MSc Thesis, Faculty of Graduate School, University of Maryland, College Park, USA, 2010.
- [17] A. Coppalle, P.E. Damay, D. Maro, M. Talbaut, O. Connan, D. Hébert, Validation of aerosols dry deposition velocity models with new data, in: 13th Conference on Harmonisation within Atmospheric Dispersion Modeling for Regulatory Purposes, Paris, France, 2010, pp. 658–661.
- [18] G. Shrestha, S.J. Traina, C.W. Swanston, Black carbon's properties and role in the environment: a comprehensive review, *Sustainability* 2 (2010) 294–320.
- [19] L.L. Alston, S. Zoledziowski, Growth of discharges on polluted insulators, *Proceedings of IEE* 110 (1963) 1260–1266.
- [20] B.F. Hampton, Flashover mechanism of polluted insulation, *Proceedings of IEE* 111 (1964) 900–985.
- [21] H. Boheme, F. Obenaus, Pollution flashover tests on insulators in the laboratory and in systems and the model concept of creepage path flashover, *Cigré* (1966), paper 407.
- [22] R. Wilkins, Flashover voltage of high voltage insulators with uniform surface pollution films, *Proceedings of IEE* 116 (1969) 457–465.
- [23] F.A.M. Rizk, Mathematical models for pollution flashover, *Electra* 78 (1981) 71–103.
- [24] R. Sundararajan, R.S. Gorur, Dynamic arc modeling of pollution flashover of insulators under dc voltage, *IEEE Transactions on Electrical Insulation* 28 (1993) 209–218.
- [25] R. Sundararajan, N.R. Sathureddy, R.S. Gorur, Computer-aided design of porcelain insulators under polluted conditions, *IEEE Transactions on Dielectrics and Electrical Insulation* 2 (1995) 121–127.
- [26] N. Dhahbi-Megriche, A. Beroual, Flashover dynamic model of polluted insulators under ac voltage, *IEEE Transactions on Dielectrics and Electrical Insulation* 7 (2000) 283–289.
- [27] R. Boudissa, S. Djafri, A. Haddad, R. Belaicha, R. Bearsch, Effect of insulator shape on surface discharges and flashover under polluted conditions, *IEEE Transactions on Dielectrics and Electrical Insulation* 12 (2005) 429–437.
- [28] M.T. Gencoglu, M. Cebeci, Computation of AC flashover voltage of polluted HV insulators using a dynamic arc model, *European Transactions on Electrical Power* 10 (2008) 249–262.
- [29] T.C. Chen, H.I.M. Nour, A study on the profile of HVDC insulators, *IEEE Transactions on Electrical Insulation* 24 (1989) 113–117.
- [30] T.C. Chen, H.I.M. Nour, C.Y. Wu, DC interfacial breakdown on contaminated electrolytic surfaces, *IEEE Transactions on Electrical Insulation* 19 (1984) 536–542.
- [31] H.A.M. Al-Nehari, A study on the effects of air pollutants and dispersion in urban atmospheres, PhD Thesis, Department of Mechanical Engineering, Faculty of Engineering, Assiut University, Assiut, Egypt, 2010.
- [32] F.P. Incropera, D.P. Dewitt, *Introduction to Heat Transfer*, 3rd ed., Wiley, NY, 1992.
- [33] H. Singer, H. Steinbigler, P. Weiss, A charge simulation method for the calculation of high voltage fields, *IEEE Transactions on PAS* 93 (1974) 1660–1668.
- [34] T. Takuma, T. Kawamoto, Field calculation including surface resistance by charge simulation method, in: 3rd Int. Symp. on HV Eng., Milan, Italy, 1979, paper no. 12–01.
- [35] T. Takuma, T. Kawamoto, H. Fujinami, Charge simulation method with complex fictitious charges for calculating capacitive-resistive fields, *IEEE Transactions on PAS* 100 (1981) 4665–4672.
- [36] F. Gutfleisch, Berechnung elektrischer Felder durch Nachbildung der Grenzschichten mit ausgewählten Flächenelementen, Diss. Technischen Universität Hamburg-Harburg, 1989.
- [37] G.G. Karady, F. Amrah, Dynamic modeling of AC insulator flashover characteristics, in: IEE Symposium on High Voltage Engineering, No. 467, August, 1999, pp. 107–110.
- [38] S.V. Patankar, *Numerical Heat Transfer and Fluid Flow*, Hemisphere Publishing Corporation, NY, 1980.
- [39] D. Balsara, Fast and accurate discrete ordinates methods for multidimensional radiative transfer. Part I, basic methods, *Journal of Quantitative Spectroscopy and Radiative Transfer* 69 (2001) 671–707.
- [40] G. Xu, P.B. McGrath, Electrical and thermal analysis of polymer insulator under contaminated surface conditions, *IEEE Transactions on Dielectrics and Electrical Insulation* 3 (2) (1996) 289–298.
- [41] S. Chakravorti, P.K. Mukherjee, Power frequency and impulse field calculation around a HV insulator with uniform or nonuniform surface pollution, *IEEE Transactions on Electrical Insulation* 28 (1) (1993) 43–53.
- [42] E.M.M. El-Refai, M.T. El-Noaman, M.K. Mohamed, Dynamic arc modeling of pollution flashover process on HV insulators under AC voltage, in: 13th Middle East Power Systems Conference, MEPCON'09, Assiut University, Egypt, 2009, pp. 662–667.